COLLECTIVE SCATTERING AND ABSORPTION EFFECTS IN MICROWAVE INTERACTION WITH VEGETATION CANOPIES

W. C. Au, L. Tsang, R. T. Shin, and J. A. Kong

1.   Introduction

In a vegetation canopy, branches and leaves occur in random clusters rather than in a uniform random distribution. In this chapter , we study the collective scattering and absorption effects of a conglomeration of particles. The radiative transfer theory is modified by defining the phase matrix and extinction coefficient as respectively, the bistatic cross section per unit volume of space and the extinction cross section per unit volume of space. The limit of the volume of space is taken such that it is much larger than a wavelength and contains many particles so that the collective scattering effects of the particles within the volume are taken into account [1]. In this chapter, for the scatterers enclosed within the volume of space , we solve Maxwell's equations exactly by using the method of moments to calculate the collective scattering and absorption behavior. The results between this new theory and the classical radiative transfer theory will be compared.

Classical vector radiative transfer theory (RT) has been used extensively in studying the electromagnetic scattering effects in microwave remote sensing [2–5]. However, classical radiative transfer theory assumes that the particles scatter independently. This assumption is based on the random phase of scattering by different particles and is valid if the particle positions are independent and the randomness of relative positions is comparable to or larger than a wavelength. Such an assumption can be invalid for microwave scattering by terrains. For example, in dense media with particles closely packed together as grains in snow and ice, and for scatterers clustered together as in branches and leaves in a vegetation canopy, the randomness of relative positions of scatterers can be less than a wavelength. In such a case, the scatterers scatter collectively. Collective scattering effects include correlated scattering, taking into account the relative phase of scattered waves from the scatterers and its neighbors. The mutual coherent wave interaction between scatterers are also to be included [5–7].

The collective scattering behavior of branching vegetation was first studied by Yueh et al [8]. In the coherent addition approximation (coherent scattering) model, the internal fields of the scatterers like branches and leaves are assumed to be the same as that of independent scattering. Mutual interactions are ignored. The collective scattering behavior is then taken into account by including the relative phase shifts of the scatterered fields from different scatterers due to their rel-

ative positions with each other. A significant difference compared to the independent scattering model was observed [8–10]. However, the model does not account for the coherent multiple scattering between different scatterers. Also, since the internal field in the model is assumed to be the same as that of independent scattering, the absorption coefficients remain unchanged. When the mutual coherent interaction is taken into account, the absorption coefficients can be significantly different [11,12]. In this chapter, coherent interaction model (full numerical model) is proposed, in which numerically exact solutions of Maxwell's equations are obtained within the volume of space of many scatterers and average over many realizations is taken. Recently, Monte Carlo simulation of solutions of Maxwell's equations has become an important procedure for random media problems. Such Monte Carlo simulations have been applied to random one- dimensional and two-dimensional random rough surface simulations [13,14] and dense media simulations [15,16].

For uniform dense media, for example, snow and ice, the fractional volume of the scatterers is more than 20% and the collective scattering effects can be described by the dense media theory [2,7]. In vegetation canopies, the fractional volume of particles is low, usually between 0.1% to 0.5%. However, the scatterers occur in clusters. In this chapter, we study the collective scattering and absorption effects of a conglomeration of particles in clusters. In Section 2, we calculate the numerical solution of scattering by dielectric cylindrical clusters. Integral equations are formulated with the method of moments (MoM), discrete dipole approximation and thin dielectric cylinder approximation. Good agreement between the model and experimental data is obtained at X-band frequency. In Section 3, we formulate the vector radiative transfer theory with collective scattering effects. The phase matrix and extinction matrix are redefined by using many scatterers and using the per unit volume concept. The limit of the volume of space is taken such that it is much larger than a wavelength and contains many particles so that the collective scattering effects within the volume are taken into account. In Section 4, the vector radiative transfer theory result is applied to that of active remote sensing. It is shown that the coherent addition approximation, which accounts for the coherent scattering effect while neglecting the multiple scattering effect on the induced currents on the cylinder, provides a good estimate for co-polarized returns. For cross-polarized returns, both the

independent scattering and coherent addition approximation models are shown to be less accurate. Cross-polarized returns are strongly influenced by interactions between the components of the cluster and the approximate methods do not account for this effect. In Section 5, it is applied to that of passive remote sensing. The radiative transfer equations for passive remote sensing are solved numerically by the discrete eigenanalysis method, which accounts for the multiple scattering effects. The brightness temperatures of the random medium containing discrete vegetation clusters overlying the planar bottom surfaces are calculated. Numerical results show that the coherent addition approximation gives a better estimate of the brightness temperatures than the independent scattering model for half-space cases. Both the independent scattering and coherent addition approximation models underestimate the optical depth of the random medium layer.

2.   Numerical Solution of Scattering by Clusters of Thin Dielectric Cylinders

Electromagnetic scattering from dielectric scatterers have been a subject of interest for many years because of their wide range of applications. A variety of techniques have been developed for analyzing electromagnetic scattering by objects of different shapes and properties. In this section, we apply the volume integral equation method. In volume integral methods, the unknowns in the problem are expressed in terms of volume currents flowing inside the bodies. The volume current consists of the conduction current as well as the displacement current induced by the total field. The volume integral equation is then approximated by a matrix equation.

We apply the volume integral method to solve thin dielectric structures with applications in remote sensing. A thin dielectric cylinder structure model is used to simulate natural vegetation canopy of bare twigs of deciduous trees and needle-shaped leaves of coniferous trees. Averaging over orientations of different realizations is necessary in order to obtain reliable results.

In Section 2.1, the volume integral formulation is discussed. The discussion is then followed by the method of solution in Section 2.2 which gives details of the formation of the matrix equation. Numerical results are presented and comparisons with experimental data is made in Section 2.3.

2.1 Formulation

In this section, the formulation of the volume integral equation of the electric field is derived from Maxwell's equations [17]. The volume integral equation is well suited for solving scattering problems of inhomogeneous bodies. In Fig. 1, a scatterer of volume V, permittivity ϵ and permeability μ is in region V_1 bounded by the surface S_1, which may be infinitely large.
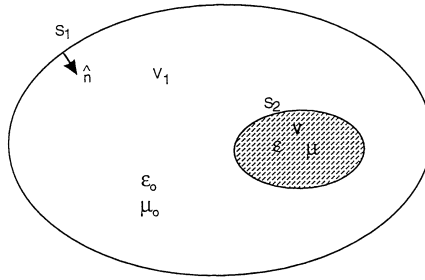

Figure 1. Scattering problem for an inhomogeneous material body.

The scatterer can be replaced by equivalent electric and magnetic volume currents $\overline{J}_{eq}$ and $\overline{M}_{eq}$ in the following way. In the presence of the scatterer, we have

$$\nabla \times \overline{H} = -i\omega\epsilon\overline{E} + \overline{J} \tag{1}$$
$$\nabla \times \overline{E} = i\omega\mu\overline{H} - \overline{M} \tag{2}$$

By replacing the scatterer with $\overline{J}_{eq}$ and $\overline{M}_{eq}$

$$\nabla \times \overline{H} = -i\omega\epsilon_o\overline{E} + \overline{J}_{eq} + \overline{J} \tag{3}$$
$$\nabla \times \overline{E} = i\omega\mu_o\overline{H} - \overline{M}_{eq} - \overline{M} \tag{4}$$

For equations (1) and (2) to be equivalent to equations (3) and (4), we need

$$\overline{J}_{eq} = -i\omega(\epsilon - \epsilon_o)\overline{E} \tag{5}$$
$$\overline{M}_{eq} = -i\omega(\mu - \mu_o)\overline{H} \tag{6}$$

Equations (5) and (6) state the volume equivalence theorem which is valid for material bodies that are inhomogeneous since ϵ and μ

can be a function of position $\overline{r}$. With the equivalent currents, the scattered fields can be expressed in terms of $\overline{\overline{G}}_e$ and $\overline{\overline{G}}_m$, which are the electric and magnetic dyadic Green's functions subject to the boundary conditions [18].

$$\overline{E}^s = i\omega\mu \int_V \overline{\overline{G}}_e \cdot \overline{J}_{eq} \, dv^{'} - \int_V \overline{\overline{G}}_m \cdot \overline{M}_{eq} \, dv^{'} \tag{7}$$

$$\overline{H}^s = i\omega\epsilon \int_V \overline{\overline{G}}_e \cdot \overline{M}_{eq} \, dv^{'} + \int_V \overline{\overline{G}}_m \cdot \overline{J}_{eq} \, dv^{'} \tag{8}$$

The total fields $\overline{E}$ and $\overline{H}$ are equal to the sum of the incident and the scattered fields.

$$\overline{E} = \overline{E}^i + \overline{E}^s \tag{9}$$

$$\overline{H} = \overline{H}^i + \overline{H}^s \tag{10}$$

Substituting equations (7) and (8) into equations (9) and (10), we obtain the following volume integral equations.

$$\overline{E} = \overline{E}^i + i\omega\mu \int_V \overline{\overline{G}}_e \cdot \overline{J}_{eq} \, dv^{'} - \int_V \overline{\overline{G}}_m \cdot \overline{M}_{eq} \, dv^{'} \tag{11}$$

$$\overline{H} = \overline{H}^i + i\omega\epsilon \int_V \overline{\overline{G}}_e \cdot \overline{M}_{eq} \, dv^{'} + \int_V \overline{\overline{G}}_m \cdot \overline{J}_{eq} \, dv^{'} \tag{12}$$

Now we let S_1 recede to infinity so that the region V_1 becomes unbounded. The Green's functions can be expressed as

$$\overline{\overline{G}}_e(\overline{r}, \overline{r}') = (\overline{\overline{I}} + \frac{1}{k^2}\nabla\nabla)g(\overline{r}, \overline{r}') \tag{13}$$

$$\overline{\overline{G}}_m(\overline{r}, \overline{r}') = \nabla \times [\overline{\overline{I}}g(\overline{r}, \overline{r}')] \tag{14}$$

where $\overline{\overline{I}}$ is the identity matrix and $g(\overline{r}, \overline{r}')$ is the scalar Green's function given by

$$g(\overline{r}, \overline{r}') = \frac{e^{ik|\overline{r}-\overline{r}'|}}{4\pi|\overline{r} - \overline{r}'|} \tag{15}$$

For scattering problem of a dielectric body of permittivity ϵ and permeability μ_o, we have

$$\overline{J}_{eq} = i\omega(\epsilon_o - \epsilon)\overline{E} \tag{16}$$

$$\overline{M}_{eq} = 0 \tag{17}$$

Substituting into equation (11), we obtain

$$\frac{\overline{J}_{eq}}{i\omega(\epsilon_o - \epsilon)} - i\omega\mu_o \int_V \overline{\overline{G}}_e \cdot \overline{J}_{eq}\, dv' = \overline{E}^i \tag{18}$$

where V is the volume of the scatterer. This is a Fredholm integral equation of the second kind, in which the unknown $\overline{J}_{eq}$ is present both inside and outside the integral.

2.2. Method of Solution

Point Matching Method.

To solve equation (18), moment method with a point matching as testing is used. $\overline{J}_{eq}(\overline{r})$ is expressed in a set of basis functions, $\overline{B}_j(\overline{r})$, defined as

$$\overline{B}_j(\overline{r}) = \sum_{k=1}^{3} \hat{u}_k P_j(\overline{r}) \tag{19}$$

where

$$P_j(\overline{r}) = \begin{cases} 1 & \text{for } \overline{r} \in V_j \\ 0 & \text{otherwise} \end{cases} \tag{20}$$

and $\hat{u}_k$ denotes unit vectors $\hat{x}$, $\hat{y}$, and $\hat{z}$ in a rectangular coordinate system. The scatterer is divided into N subvolumes, in which the equivalent current is assumed to be constant. Thus

$$\overline{J}_{eq}(\overline{r}) = \sum_{j=1}^{N}\sum_{k=1}^{3} \alpha_{jk}(\overline{B}_j(\overline{r}) \cdot \hat{u}_k)\hat{u}_k \tag{21}$$

Discretizing $\overline{J}_{eq}$ in terms of the basis functions, equation (18) can be expressed in a compact form,

$$\sum_{j=1}^{N}\sum_{k=1}^{3} \alpha_{jk}\overline{\overline{L}}(B_j^k(\overline{r})) = \overline{E}^i(\overline{r}) \tag{22}$$

where

$$\overline{\overline{L}} \cdot \overline{J} = \frac{\overline{\overline{I}} \cdot \overline{J}}{i\omega(\epsilon_o - \epsilon)} - \int_V i\omega\mu_o\overline{\overline{G}}_e \cdot \overline{J}\, dv'$$

and

$$B_j^k = (\overline{B}_j(\overline{r}) \cdot \hat{u}_k)\hat{u}_k$$

To determine $3N$ unknown α's, a delta weighting function (thus, the term point matching) is used to form the matrix equations.

$$\overline{W}_p^n = \delta(\overline{r} - \overline{r}_p)\hat{u}_n \tag{23}$$

where $\overline{r}_p$ is a representative point inside the subvolume V_p.

Taking the inner product of equation (22), we get

$$\sum_{j=1}^{N}\sum_{k=1}^{3} \alpha_{jk} Z_{jk}^{pn} = V^{pn} \tag{24}$$

where

$$Z_{jk}^{pn} = <\overline{W}_p^n, \overline{\overline{L}}B_{jk}>$$
$$V^{pn} = <\overline{W}_p^n, E_n^i \hat{u}_n> = E_n^i(\overline{r}_p)$$
$$<\overline{f},\overline{g}> = \int_V \overline{f} \cdot \overline{g}\,dv$$

Numerical Evaluation of Matrix Elements

To calculate the matrix elements Z in equation (24), the singularity of the Green's function must be handled with care. The problem of handling the singularity of the Green's functions has been addressed in the literature [19, 20]. Difficulties with the numerical evaluation of the Green's function of an infinitesimally small volume has also been reported [21]. For this reason, we choose to use a finite size exclusion volume in the calculation.

Thin Cylinder Considerations

A computer code (THINC) is developed primarily for electrically thin cylinder structures, i.e. $ka \ll 1$, k being the free space wavenumber and a the representative radius of the cylinder structure. In the discretization process, the structure is divided into cylindrically shaped subcells. It is then natural to use an exclusion volume of cylindrical shape. The exclusion volume is chosen to be a cylinder of radius a and length b, where b is the minimum of the length of the cylindrical subcell and one fortieth of the wavelength [22]. The matrix elements for

non-diagonal terms can be evaluated by discrete dipole approximation [23], i.e.

$$
\begin{aligned}
I_{mn} &= \int_{V_n} \overline{\overline{G}}(\overline{r}, \overline{r}') \cdot \overline{J} dV' \\
&\approx G_{x_p x_q}(\overline{r}_m, \overline{r}_n) \Delta V_n
\end{aligned}
\tag{25}
$$

where

$$
G_{x_p x_q}(\overline{r}, \overline{r}') = i\omega\mu_o (\delta_{pq} + \frac{1}{k^2} \frac{\partial^2}{\partial x_p \partial x_q}) g(\overline{r}, \overline{r}') J_q(\overline{r}')
\tag{26}
$$

when two subcells m and n are far apart. When m and n are close to each other, numerical integration must be carried out to evaluate I_{mn}.

2.3 Results and Discussion

The numerical results are first verified by comparing to results from another method of moments code for a body of revolution based on the surface integral formulation [24]. The observation of the optical theorem (as known as extinction theorem) is also checked. After that, the computer code is applied to model branching vegetation clusters. The theoretical results are then compared with experimental data.

The backscattering cross sections of a cylinder of permittivity $\epsilon = (3 + i0.5)\epsilon_o$, length $l = \lambda$, radius $a = \lambda/10$ at 3 GHz as a function of incidence angle are shown in Figs. 2 and 3.

The results agree very well with that from the body of revolution code. In Figs. 4 and 5, the total scattering cross section, absorption cross section, their sum and the extinction cross section are plotted for the same cylinder.

The extinction cross section is calculated from the optical theorem given by [2]

$$
\sigma_{epp} = \frac{4\pi}{k_o} \text{Im}\{f_{pp}(\theta_i, \theta_i)\}, \qquad p = v, h
\tag{27}
$$

where k_o is the free space wavenumber, f_{pp} is the scattering function. By energy conservation, the extinction cross section is equal to sum of the absorption and the total scattering cross sections.
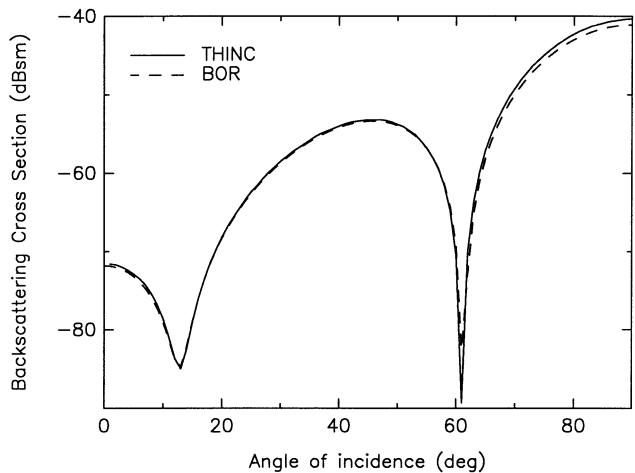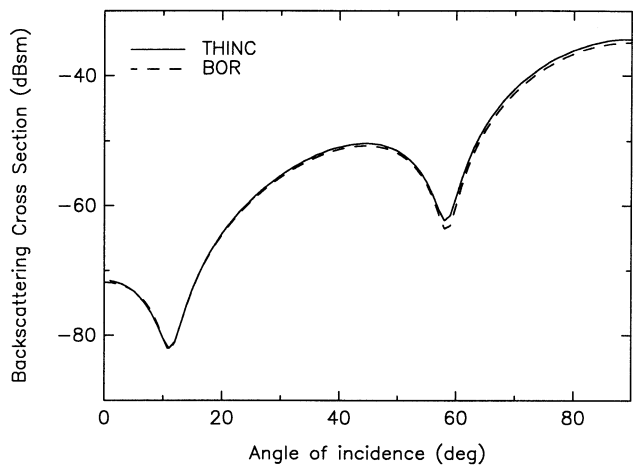
Figure 2. Comparison of backscattering cross sections as a function of incidence angle as computed by **THINC** and body of revolution code using surface integral approach. Cylinder length $l = 10$cm, radius $r = 0.5$cm, and $\epsilon = (3 + i0.5)\epsilon_0$ at **3GHz** for horizontal polarization.

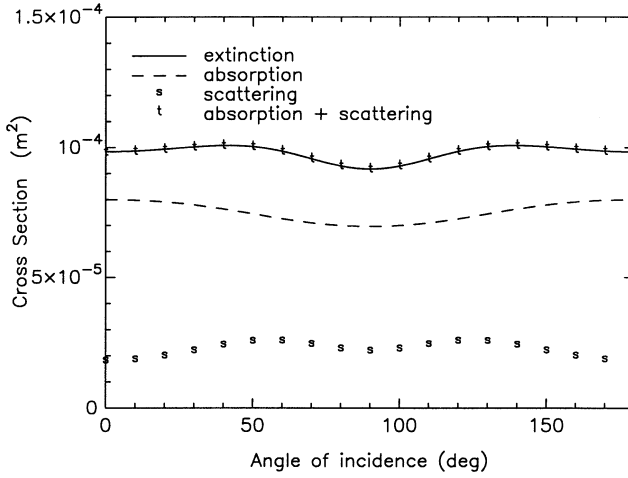**Figure 3.** Comparison of backscattering cross sections as a function of incidence angle as computed by **THINC** and body of revolution code using surface integral approach. Cylinder length $l = 10$cm, radius $r = 0.5$cm, and $\epsilon = (3 + i0.5)\epsilon_0$ at **3GHz** for vertical polarization.

Figure 4. Absorption, extinction, and total scattering cross sections as a function of incidence angle for a cylinder of length $l = 10$cm, radius $r = 0.5$cm, and $\epsilon = (3 + i0.5)\epsilon_0$ at 3GHz for horizontal polarization.
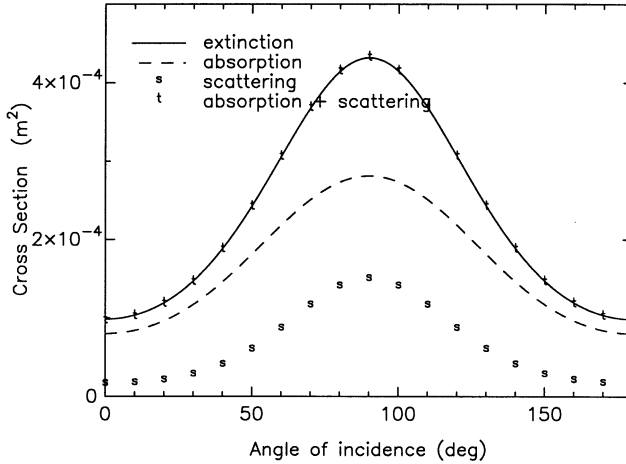

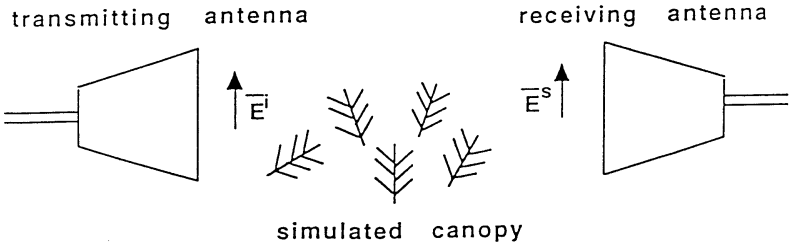**Figure 5. Absorption, extinction, and total scattering cross sections as a function of incidence angle for a cylinder of length $l = 10$cm, radius $r = 0.5$cm, and $\epsilon = (3 + i0.5)\epsilon_0$ at 3GHz for vertical polarization.**

transmitting   antenna   receiving   antenna

$\overline{E}^i$ $\overline{E}^s$

simulated   canopy

Figure 6. Experiment setup for microwave coherent propagation in cylindrically shaped forest components [25].

The theory is then applied to model vegetation clusters. The theoretical results are compared with X-band experiments on cylindrically shaped forest components [25]. The experiment was carried out under laboratory conditions in which the parameters of the vegetation components can be measured and controlled. Transmission measurements were performed on simulated canopies composed of bare deciduous twigs and leafy coniferous branches at 9 GHz. The system consisted of a transmitting and a receiving antenna. The antennas were linearly polarized. The vertically oriented vegetation samples were placed on a Styrofoam frame in one or several rows between the two antennas (Fig. 6). Parameters for the samples are given in Table 1.

Needle azimuth distribution	quasi uniform
Needle elevation distribution	extremophile 45°
Needle length	1.8cm
Needle thickness	0.8mm
Needle width	1.2mm
Needle density	13.9/cm
twig diameter	0.36cm

Table 1. Characteristics of the Norway spruce needles [25].

Measurements were performed with vegetative targets and the transmitted powers were recorded. Different samples were used and averaged to give the received power P_1. After removing the targets, the reference power P_o was then recorded. The loss factor, $L(\theta_i, p)$, is defined as the one way transmission loss of the vegetation canopy for the incidence angle θ_i with a polarization angle p, such that

$$L(\theta_i, p) = 10 \log \frac{P_o}{P_1} \tag{28}$$

For the theoretical calculation, Foldy's approximation [2,26,27] is employed to account for the attenuation introduced by the medium. The propagation of the coherent wave with E_h and E_v as the horizontal and the vertical components of the electric field is governed by the following equations:

$$\frac{dE_v}{ds} = (ik_o + M_{vv})E_v + M_{vh}E_h \tag{29}$$

$$\frac{dE_h}{ds} = M_{hv}E_v + (ik_o + M_{hh})E_h \tag{30}$$

where s is the distance along the direction of propagation, and

$$M_{jl} = \frac{i2\pi n_o}{k_o} < f_{jl}(\theta, \phi; \theta, \phi) > \qquad j, l = v, h \tag{31}$$

with (θ, ϕ) as the direction of propagation, n_o the number density of the scatterers, and $<>$ denotes ensemble average over the orientation and size distribution of the scatterers. For vegetation canopy that exhibits azimuthal symmetry, there is no coupling between the horizontal and vertical components of the coherent field. Hence the cross-polarized components M_{hv} and M_{vh} are zero. The effective propagation constants are given by

$$k_p = k_o - iM_{pp} \qquad p = v, h \tag{32}$$

The effective propagation constants are then used to calculate the loss factor [28]. The received power for a linearly polarized wave transmitted through the medium with the effective propagation given in (32) at the incidence angle of θ_i is given by

$$P_r = C_r | \cos \psi_i \cos \psi_r e^{-i\delta_v d/\cos\theta_i} + \sin \psi_i \sin \psi_r e^{-i\delta_h d/\cos\theta_i} |^2$$

where

$$C_r = \frac{1}{\eta_o} G_r \frac{\lambda_o^2}{4\pi} \tag{34}$$

$$\delta_p = iM_{pp} \qquad p = v, h \tag{35}$$

and G_r is the gain, η_o is the intrinsic wave impedance, λ_o is the wavelength, d is the depth of the medium, and ψ_i and ψ_r are respectively the polarization angles for the incident wave and the receiving antenna. The reference received power is measured with the vegetative target removed, i.e. δ_p are zero. The loss factor for the co-polarized transmitted field is measured with $\psi_i = \psi_r$ and is given as

$$L(\theta_i, \psi_i) = | \cos^2 \psi_i e^{-\kappa_{ev} d/2 \cos\theta_i} + \sin^2 \psi_i e^{-\kappa_{eh} d/2 \cos\theta_i} e^{i\Delta\beta d/\cos\theta_i} |^{-2} \tag{36}$$

where

$$\kappa_{ep}(\theta_i) = \frac{4\pi}{k_o} n_o \operatorname{Im}(< f_{pp}(\theta; \theta) >) \tag{37}$$

and

$$\Delta\beta = (2\pi/k_o) n_o [Re(< f_{hh}(\theta; \theta) >) - Re(< f_{vv}(\theta; \theta) >)] \tag{38}$$

The dielectric constant of the leaves is determined using the Ulaby and El Rayes' model [29] according to the water content of the leaves reported in reference [25]. The method of moments code is used to calculate the scattering function of the vegetation samples. Realizations of the vegetation sample are made according to the parameters given in Table 1.

Averaging over different realizations is taken to obtain average scattering amplitudes. In Fig. 7, we show the comparison of the theoretical calculation and experimental data for the attenuation of vertically oriented bare twigs as a function of incidence angle. Good agreement is observed. In Fig. 8 we compare the theoretical loss factors with the

measurements as a function of the polarization angles at an incidence angle of 90° for Norway spruce leaves.

For the calculation, the needles are assumed to be entirely responsible for the measured attenuation. Hence only the needle characteristics are incorporated in the model and the central twig is neglected. The needles are assumed to have the same circular cross section with radius a. The needle orientation was estimated [25] and the probability density function is used to generate a vegetation sample. The clustering effect is accounted for. The position and the orientation of each component are generated by Monte Carlo method and self-avoidance of each component is checked. Only the center one third portion of the structure is used in the calculation due to the limitation of computer resource. The number of twigs used in the vegetative target is not reported, therefore only a qualitative study is carried out. The theoretical curve is adjusted to the experimental curve by choosing a suitable number of scatterers, n_o, in equation (36). The comparison between the model and experimental data shows that the attenuation behavior of vegetation components at X-band microwaves can be predicted reasonably well by scattering functions obtained from the method of moments calculation.
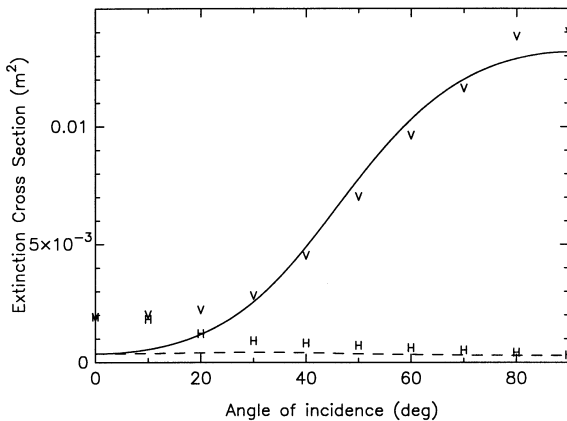

Figure 7. Comparison of the theoretical extinction cross section of bare twigs and experimental data as a function of the incidence angle θ_i for a cylinder of length 10 cm, radius 1.5 mm, at 9GHz. ϵ is chosen to be $(11 + i4)\epsilon_0$.

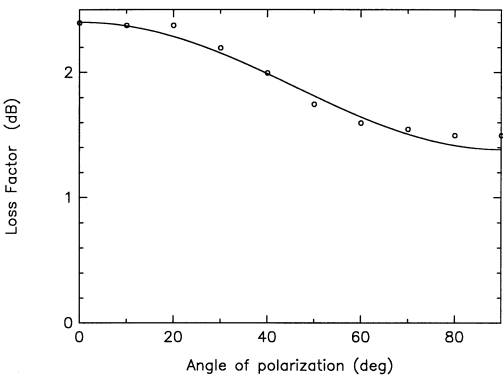**Figure 8. Comparison of the theoretical loss factor and measurements as a function of the polarization angle ψ_i, $(\theta = 90°)$ for Norway spruce twigs.**

3.   Vector Radiative Transfer Theory with Collective Scattering Behavior of Particles

In this section, we define the radiative transfer theory that includes the collective scattering behavior of particles. This distinguishes the new definition from the conventional definition of single particle scattering behavior.

In radiative transfer theory [2], we consider a specific intensity incident upon an elemental volume with cross sectional area A and length ds (Fig. 9).
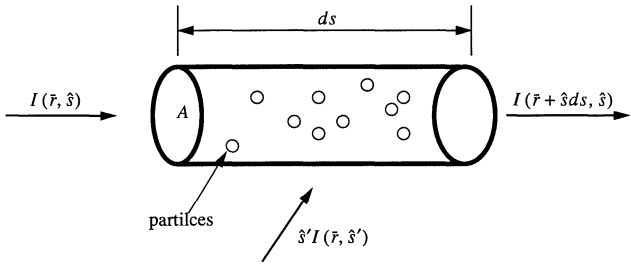
Figure 9. Elemental volume for radiative transfer equation.

The cross sectional shape is arbitrary. It is an elemental volume in the development of the radiative transfer equation. It is not small in the sense of the wave equation. Let the volume $V = A ds$ obey the following criteria

(i) $V >> \lambda^3$ where λ is the wavelength.

(ii) There is a large number of particles N, contained in V. The particles are randomly positioned.

Criteria (i) and (ii) are necessary so that coherent multiple scattering in volume V will have phase fluctuations such that the energy transfers in and out of volume V will become incoherent. Furthermore, if the particles are of different sizes, shapes, and permittivities in volume V, average particle scattering behavior will also be included in the radiative energy transfer within volume V. Criteria (i) and (ii) establish a lower limit of volume V.

Let $\overline{E}^i$ be the incident field in direction $\hat{k}_i = (\theta_i, \phi_i)$ and $\overline{E}^s$ be the scattered field from volume V of N particles.

$$\overline{E}^i = \overline{E} \exp\left(i\overline{k}_i \cdot \overline{r}\right) \tag{39}$$

The scattered field can be decomposed into coherent and incoherent fields.

$$\overline{E}^s = \langle E^s \rangle + \mathcal{E}_s \tag{40}$$

The scattered field $\overline{E}^s$ is a statistical field that contains the coherent multiple scattering within volume V and the statistics of $\overline{E}^s$ will be studied.

Inside volume V, coherent wave interactions among the particles take place. Such coherent wave interaction takes into account near field, intermediate field, and far field ranges. The ensemble averaged results yield extinction coefficients and phase matrices for radiative transfer theory which thus include collective scattering effects. It should be noted that both extinction coefficients and phase matrices are defined as quantities pertaining to scattering per unit volume. Thus, they are not single particle quantities. Nor are they defined as scattering from one particle to another single particle. The extinction coefficients and phase matrices are also defined in the limit of large V. Since a limit needs to exist for these quantities to be well defined, radiative transfer theory is interpreted as incoherent interaction among large volumes V. The volume V is arbitrary in shape, and edge effects of the volume for

particles at the edges of volume V are not important. Otherwise, the large V limit for extinction coefficients and phase matrices do not exist. Radiative transfer theory is regarded as incoherent wave interaction among volume elements. Near field between different volume elements are not important otherwise the edge effects of volume elements become important and hence the extinction coefficient and the phase matrix would not exist (Note that near field effects are important within the volume element, the effects of which have to be included in coherent wave interaction with the volume element as noted previously). Alternatively, one has to make the volume element large enough until near field interaction between volume elements are not important.

From one elemental volume V to other elemental volumes, the far field of $\overline{E}^s$ can be taken. We have

$$\overline{E}^s = F(\hat{k}_s, \hat{k}_i)\frac{\exp{(ikr)}}{r} \tag{41}$$

where $\hat{k}_s = (\theta_s, \phi_s)$ is the scattered direction. In (41), $F(\hat{k}_s, \hat{k}_i)$ represents the N particles collective scattering amplitude and includes all the coherent near field interactions among the N particles. It can be decomposed into coherent and incoherent components.

$$F(\hat{k}_s, \hat{k}_i) = \langle F(\hat{k}_s, \hat{k}_i)\rangle + \mathcal{F}(\hat{k}_s, \hat{k}_i) \tag{42}$$

The optical theorem can be applied to N scatterers which can be viewed as a unit. Thus, for the case of non-absorptive scatterers, we have,

$$\frac{4\pi}{k}\text{Im}\{F(\hat{k}_i, \hat{k}_i)\} = \int_{4\pi} d\Omega_s |F(\hat{k}_s, \hat{k}_i)|^2 \tag{43}$$

The phase function $P(\hat{k}_s, \hat{k}_i)$ and the scattering coefficient κ_s are defined as follows to take into account the collective scattering behavior of N particles.

$$P(\hat{k}_s, \hat{k}_i) = \lim_{V \to large} \frac{\langle |\mathcal{F}(\hat{k}_s, \hat{k}_i)|^2\rangle}{V} \tag{44}$$

$$\kappa_s = \int_{4\pi} d\Omega_s P(\hat{k}_s, \hat{k}_i) \tag{45}$$

The limit in equation (44) is taken for a fixed n_o where $n_o = N/V$ is the number of particles per unit volume. The results of (44) and

(45) should also be independent on the shape of volume V. Thus, the phase function and the scattering coefficient are defined as per unit volume quantities in the limit of large volume instead of single particle quantities. Note that the limit with large N and large V is taken for convergence. For the special case of independent scattering, the definitions of (44) and (45) agree with the conventional theory. The absorption coefficient is then

$$\kappa_a = \frac{W_a}{Q_i} \tag{46}$$

where W_a is the power absorbed by the N particles in volume V and Q_i is the incident flux. Thus, the absorption coefficient is the absorption cross section per unit volume in the limit of large V. The extinction coefficient is

$$\kappa_e = \kappa_a + \kappa_s \tag{47}$$

Once the phase matrix and the extinction coefficients are calculated, the radiative transfer equation assumes the following standard form

$$\frac{d}{ds} I(\overline{r}, \hat{s}) = -\kappa_e I(\overline{r}, \hat{s}) + \int_{4\pi} d\Omega' P(\hat{s}, \hat{s}') I(\overline{r}, \hat{s}') \tag{48}$$

where $I(\overline{r}, \hat{s})$ denotes the specific intensity.

To establish the upper limit of V for the definition of the phase function and the scattering coefficient, we note that if V is too large, then the definition of (44) will include the effects described in (48), and is actually the bistatic cross section of the overall medium (rather than the differential volume V in the radiative transfer equation) with multiple coherent and incoherent scattering included. Thus, the upper limit of V is that multiple scattering of incoherent waves will be excluded. Multiple scattering of incoherent waves will take place in the length scale of the mean free path l_{mfp}

$$l_{mfp} = \frac{1}{\kappa_e} \tag{49}$$

The third criterion of V is an upper limit and it is given as

(iii) $V << (\frac{1}{\kappa_e})^3$

The volume V can simultaneously satisfy criteria (i) and (iii) if the mean free path is much larger than the wavelength or the wavenumber is much larger than the extinction coefficient.

$$l_{mfp} \gg \lambda \qquad (50)$$

$$k \gg \kappa_e \qquad (51)$$

The conditions as exhibited in (50) and (51) are actually the conditions for transport-type equations to be valid. When the condition is violated so that $l_{mfp} \simeq \lambda$ (known as the Ioffe-Regel criterion), strong photon localization may take place and radiative transfer type equations will fail. For remote sensing of geophysical media, conditions of (50) and (51) are usually obeyed. For the case of independent scattering of N scatterers, $\langle| \mathcal{F}(\hat{k}_s, \hat{k}_i) |^2\rangle = N | f |^2$ so that $P(\hat{k}_s, \hat{k}_i) = n_o | f |^2$, where $n_o = N/V$ is the number of particles per unit volume and f is the single particle scattering amplitude. Thus, (44) and (45) reduce to the result of conventional radiative transfer theory.

3.1 Phase Matrix and Extinction Matrix

The vector radiative transfer equation is of the following form,

$$\cos\theta \frac{d\overline{I}(\theta, \phi, z)}{dz} = -\overline{\overline{\kappa}}_e(\theta, \phi) \cdot \overline{I}(\theta, \phi, z)$$
$$+ \int_0^{2\pi} d\phi' \int_0^{\pi} d\theta' \sin\theta' \overline{\overline{P}}(\theta, \phi; \theta', \phi') \cdot \overline{I}(\theta', \phi', z) \qquad (52)$$

where $\overline{I}(\theta, \phi, z)$ is the 4×1 Stokes vector, $\overline{\overline{\kappa}}_e(\theta, \phi)$ is the extinction matrix, and $\overline{\overline{P}}(\theta, \phi; \theta', \phi')$ is the phase matrix. The phase matrix elements are now defined as covariance of the elements of the incoherent scattering dyad of N scatterers in the limit of large V. For example,

$$P_{11}(\theta, \phi; \theta', \phi') = \lim_{V \to large} \frac{1}{V} \langle \mathcal{F}_{vv}(\hat{k}, \hat{k}') \mathcal{F}_{vv}{}^*(\hat{k}, \hat{k}') \rangle \qquad (53)$$

$$P_{12}(\theta, \phi; \theta', \phi') = \lim_{V \to large} \frac{1}{V} \langle \mathcal{F}_{vh}(\hat{k}, \hat{k}') \mathcal{F}_{vh}{}^*(\hat{k}, \hat{k}') \rangle \qquad (54)$$

$$P_{13}(\theta, \phi; \theta', \phi') = \lim_{V \to large} \frac{1}{V} Re\{ \langle \mathcal{F}_{vv}(\hat{k}, \hat{k}') \mathcal{F}_{vh}{}^*(\hat{k}, \hat{k}') \rangle \} \qquad (55)$$

with similar definitions for other phase matrix elements with one to one correspondence with that of conventional independent scattering [1]. In (53) through (55), $\hat{k}' = (\theta', \phi')$ and $\hat{k} = (\theta, \phi)$ represent, respectively, the incident and scattered directions. The absorption coefficient is

$$\kappa_{a\beta}(\theta, \phi) = \frac{W_{\alpha\beta}}{Q_{i\beta}} \tag{56}$$

where $\beta = v, h$. The extinction coefficients for vertically and horizontally polarized waves are, respectively,

$$\kappa_{ev}(\theta, \phi) = \kappa_{av}(\theta, \phi) + \int_0^{2\pi} d\phi' \int_0^{\pi} d\theta' \sin \theta' (P_{11}(\theta, \phi; \theta', \phi') \\ + P_{21}(\theta, \phi; \theta', \phi')) \tag{57}$$

$$\kappa_{eh}(\theta, \phi) = \kappa_{ah}(\theta, \phi) + \int_0^{2\pi} d\phi' \int_0^{\pi} d\theta' \sin \theta' (P_{12}(\theta, \phi; \theta', \phi') \\ + P_{22}(\theta, \phi; \theta', \phi')) \tag{58}$$

3.2 Simplification Based on Primary Scatterer Concepts

Because of the large number of scatterers in volume V, very often it is difficult to perform Monte Carlo simulations of such a large volume. A simplification can be made by using the primary scatterer concept. Considering a volume containing many clusters of scatterers, one can propose to use such a cluster as a primary scatterer. A primary scatterer needs only to obey one of the following two conditions.

(a) Each primary scatterer is randomly placed. The separation is a random quantity with a standard deviation larger than a wavelength.
(b) The primary scatterer is large compared with wavelength, which also facilitates (a).

As a result of (a) and (b), the scattering from different primary scatterers will be uncorrelated. Let $F_p(\hat{k}_s, \hat{k}_i)$ be the scattering amplitude of a primary scatterer. Then the phase function is

$$P(\hat{k}_s, \hat{k}_i) = n_o \langle |F_p(\hat{k}_s, \hat{k}_i)|^2 \rangle \tag{59}$$

where n_o is the number of primary scatterers per unit volume. The extinction coefficient is

$$\kappa_e(\hat{k}_i) = n_o \frac{4\pi}{k} Im\langle F_p(\hat{k}_i, \hat{k}_i)\rangle \qquad (60)$$

where F_p must be calculated accurately. Based on (a) and (b), the choice of primary scatterer is frequency dependent.

Considering scattering from a tree at high frequency, each branch is a primary scatterer. At lower frequency, each cluster is a primary scatterer. At even lower frequency, each tree is a primary scatterer.

4.   Applications to Active Remote Sensing

4.1 Collective Radiative Transfer Theory.

In collective radiative transfer theory, we shall assume that each cluster as illustrated in Fig. 10 as a primary scatterer. A primary scatterer is a scatterer whose scattering is uncorrelated with other scatterers.
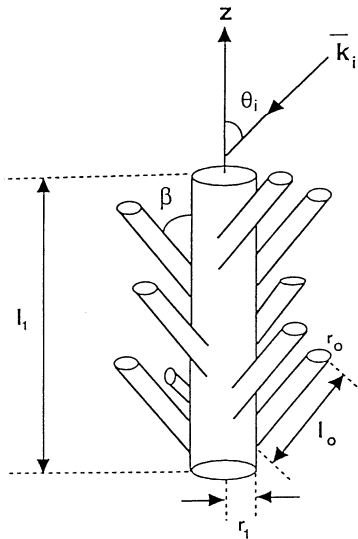
Figure 10. Configuration of the cluster. Center cylinder: length $=$ 10 cm, radius $=$ 0.3 cm; branching cylinder: length $=$ 2cm, radius $=$ 0.15 cm, branching angle $\beta = 45°$; permittivity of the cluster $= (11 + i4)\epsilon_0$; frequency is 5.3 GHz; incidence angle $= \theta_i$.

We shall compare the results for three different models. The first model is the independent scattering model. It is assumed that each branch scatters independently so that the phase matrix is the summation of the bistatic cross section for each branch. Thus

$$P(\hat{k}_s, \hat{k}_i) = n_o < |f_b(\hat{k}_s, \hat{k}_i)|^2 > \tag{61}$$

where n_o is the number of branches per unit volume and f_b is the scattering amplitude of a branch and $<>$ represents averaging over sizes and orientations. The second model is the coherent interaction model (with mutual coherent interaction included). The phase function is given as

$$P(\hat{k}_s, \hat{k}_i) = n_o < |F_p(\hat{k}_s, \hat{k}_i)|^2 > \tag{62}$$

where F_p is the scattering amplitude of a primary scatterer which is a cluster as shown in Fig. 10, n_o is the number of clusters per unit volume. In calculating F_p, the MoM code is used so that the Maxwell's equations are solved exactly to include all the coherent wave interactions among the branches of a cluster. $<>$ represents averaging over clusters. In this model, the single branch scatterer f_b is not used. The third model is the coherent addition approximation. In this model the primary scatter amplitude F_p is a coherent superposition of the single scatter amplitude f_b from each branch. The relative phase shift between different scatterers is included in this model.

$$F_p = \sum_{j}^{N} f_{bj} e^{i\theta_j} \tag{63}$$

where θ_j is the phase factor that accounts for the additional phase delay due to the relative position of the branch element and it is given as

$$\theta_j = (\overline{k}_i - \overline{k}_s) \cdot \overline{r}_j \tag{64}$$

where $\overline{r}_j$ represents the branch element location in the cluster.

4.2 Results and Discussion

In this section, theoretical results of the backscattering coefficients of the two-layer medium are presented. We consider a layer of clusters overlying a homogeneous flat dielectric surface (Fig. 11). We use first

order vector RT theory [2] to calculate the backscattering coefficients. The geometric configuration of the cylinder cluster is shown in Fig. 10. The cluster consists of a vertical center cylinder of radius 0.3 cm and of length 10 cm. There are five layers of branches distributed uniformly along the center cylinder. All the branches make an angle of 45° with the center cylinder. The radius of the branch is 0.15 cm and the length is 2 cm. Two branches are arranged in the opposite direction to each other within a layer to form a pair. This pair of branches is attached to the center cylinder at a random azimuthal position. The permittivity of the cluster is $(11 + i4)\epsilon_o$. The frequency is 5.3 GHz. The scatterer is vertically oriented.

Figures 12 and 13 show, respectively, the absorption cross section and the total scattering cross section as the function of incidence angle of a single cluster for vertical polarization.

Since the coherent addition approximation model assumes the same internal field as the independent scattering model, it has the same absorption cross section as the independent scattering model. The enhancement of the absorption is due to mutual interaction and it will be discussed in Section 5.2. For the total scattering cross section, it is observed that coherent interfence increases the scattering loss (3dB at nadir) and mutual interaction also increases the scattering loss at nadir.

With the assumption that each scatterer is far apart compared with a wavelength, the radiative transfer theory is employed to calculate the backscattering coefficients for a two-layer medium containing the scatterers. The backscattering coefficients for HH, VV and HV polarizations as a function of incidence angle are shown in Figs. 14 through 16. The scatterers are vertically oriented and the ensemble average is taken over the orientation angle (γ) of the scatterers. It is observed that the coherent addition approximation gives good estimates of the co-polarized returns (HH and VV). The difference between the approximate methods and the coherent interaction model is larger for the case of cross-polarized returns. This is because the interactions between branches and the center cylinder give rise to cross-polarized returns which cannot be captured in the approximate methods.
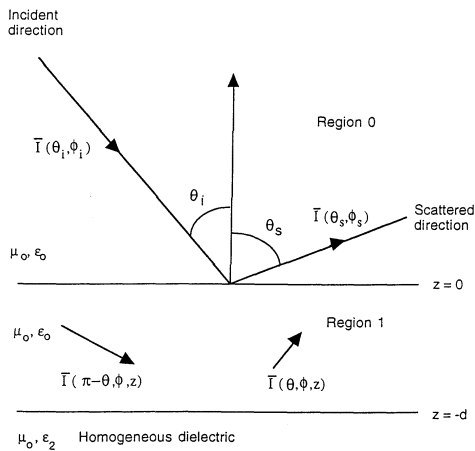
Figure 11. Configuration of two layer medium with planar interfaces containing discrete scatterers.
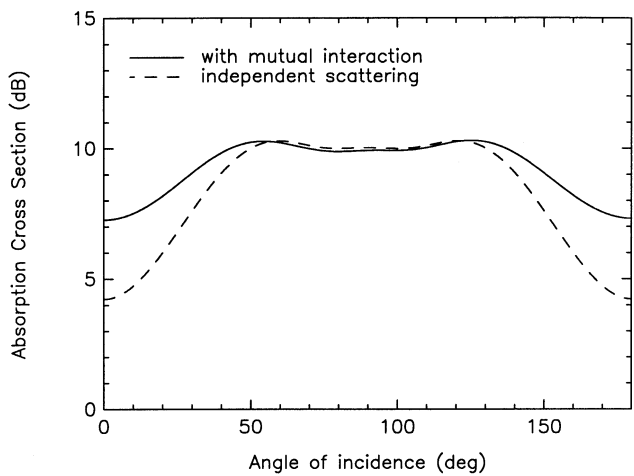

Figure 12. Absorption cross section as a function of incidence angle for vertical polarization. Number of branches is 10. Curves are normalized by $(\sigma_{ah}(90°))_{ind}$ with the numerical value of -39.5 dBsm. Frequency is 5.3 GHz.
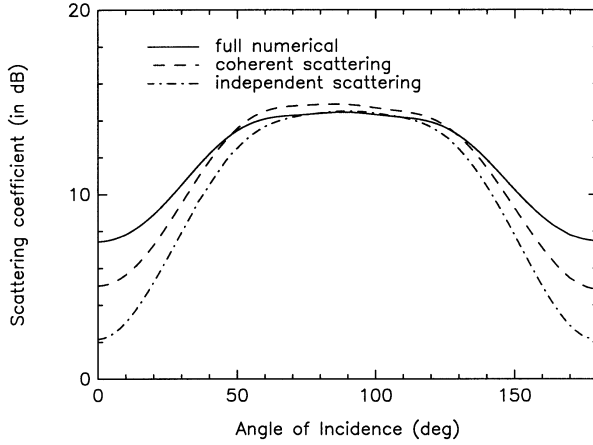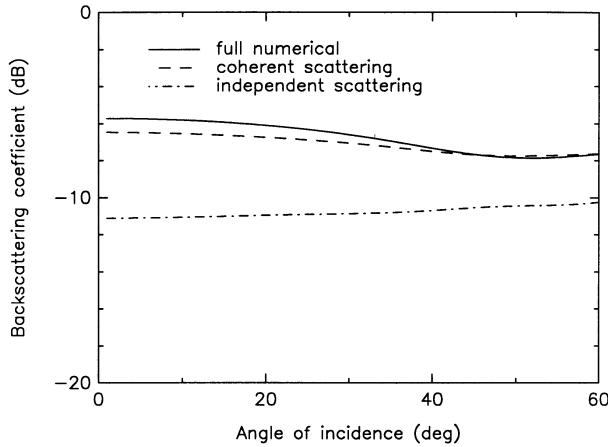
Figure 13. Scattering coefficient as a function of incidence angle for vertical polarization. Number of branches is 10. Curves are normalized by $(\sigma_{sh}(90°))_{ind}$ with the numerical value of -43.2 dBsm. Frequency is 5.3 GHz.

Figure 14. Backscattering coefficients for a two-layer medium $-\sigma_{hh}$, fractional volume $f = 0.5\%, \epsilon_s = (11+i4)\epsilon_0$. The scattering layer has a thickness $d = 0.25$ m and underlying half-space is flat and has permittivity $\epsilon_{soil} = (10+i2)\epsilon_0$. Frequency is 5.3 GHz. Number of branches for the scatterers is 10.
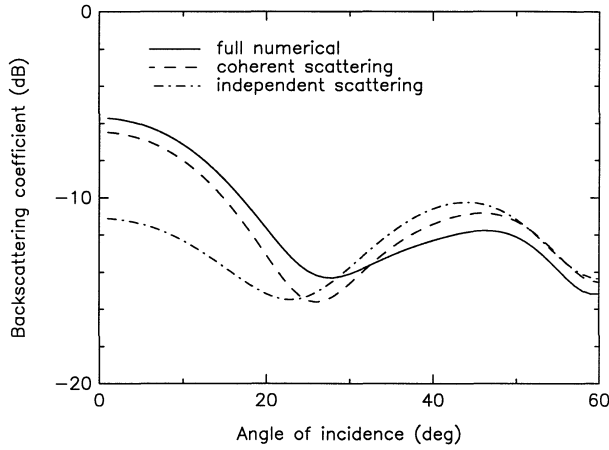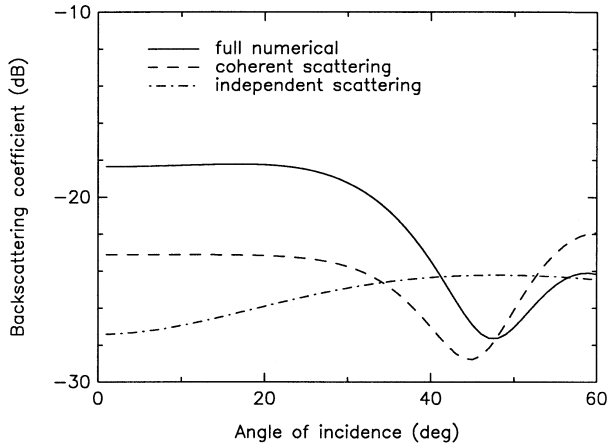
Figure 15. Backscattering coefficients for a two-layer medium $-\sigma_{vv}$**, fractional volume** $f = 0.5\%, \epsilon_s = (11+i4)\epsilon_0$**. The scattering layer has a thickness** $d = 0.25$ **m and underlying half-space is flat and has permittivity** $\epsilon_{soil} = (10+i2)\epsilon_0$**. Frequency is 5.3 GHz. Number of branches for the scatterers is 10.**

Figure 16. Backscattering coefficients for a two-layer medium $-\sigma_{hv}$**, fractional volume** $f = 0.5\%, \epsilon_s = (11+i4)\epsilon_0$**. The scattering layer has a thickness** $d = 0.25$ **m and underlying half-space is flat and has permittivity** $\epsilon_{soil} = (10+i2)\epsilon_0$**. Frequency is 5.3 GHz. Number of branches for the scatterers is 10.**

To study the cross-polarized returns for the branching cluster, the branching angle of the scatterer is varied from 10 degrees to 90 degrees. The special case of 0 degree branching angle required a slight modification of the specification of the input file to define the cluster because using the center line to define the positions of the center cylinder and branches results in overlapping the branches and the center cylinder. A slight offset of branches is needed. The cross-polarized return at nadir is zero in this case. The cross-polarized returns at nadir as a function of the branching angle is shown in Fig. 17.

With small branching angles, the depolarization effect is small. The general trend is that the cross-polarized return increases with the branching angle. It is observed that there is larger discrepancy between the coherent interaction model results and the approximate results for smaller branching angles. This is because mutual interaction is important for cross-polarized returns, which is not accounted for by the approximate methods.

At larger branching angles, a single component can give a significant cross-polarized return and the mutual interaction is less important in this case. To investigate the mechanism which accounts for the large different in cross-polarized returns, a calculation is carried out with the center cylinders of different radii. The results of the cross-polarized returns at nadir are shown in Fig. 18.

The branching angle is chosen to be 10 degrees. The coherent addition approximation and the independent scattering model give lower cross-polarized returns than the coherent interaction solution. The difference becomes larger for larger center cylinder. Both approximate methods have a lower cross-polarized return with larger center cylinder. This is due to the increase in attenuation with cylinder size and little cross-polarized contribution from the center cylinder. The results also show that the presence of the center cylinder is important for high cross-polarized returns. Since the center cylinder itself cannot give rise to high cross-polarized returns, the mechanism responsible for the high cross-polarized returns is the branch-center cylinder interaction. The wave bounces from branch to center cylinder back to other branches and gives high cross-polarized returns.
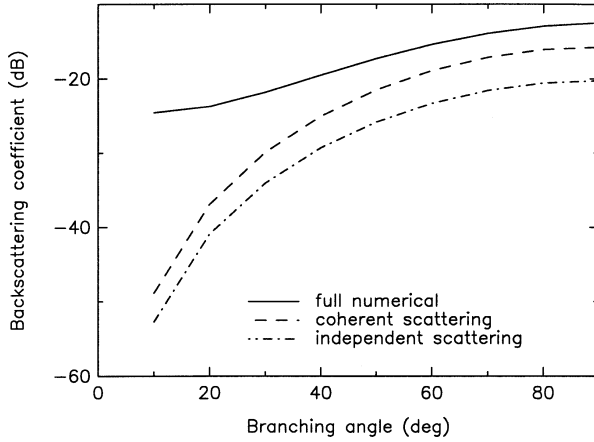
Figure 17. Backscattering coefficients for a two-layer medium $-\sigma_{hv}$ at nadir, as a function of branching angle β. Fractional volume $f = 0.5\%$, $\epsilon_s = (11 + i4)\epsilon_0$. The scattering layer has a thickness $d = 0.25$ m and underlying half-space is flat and has permittivity $\epsilon_{soil} = (10 + i2)\epsilon_0$. Frequency is 5.3 GHz. Number of branches for the scatterers is 10.
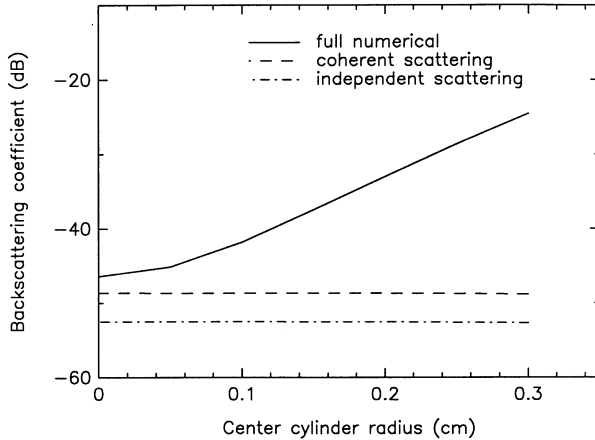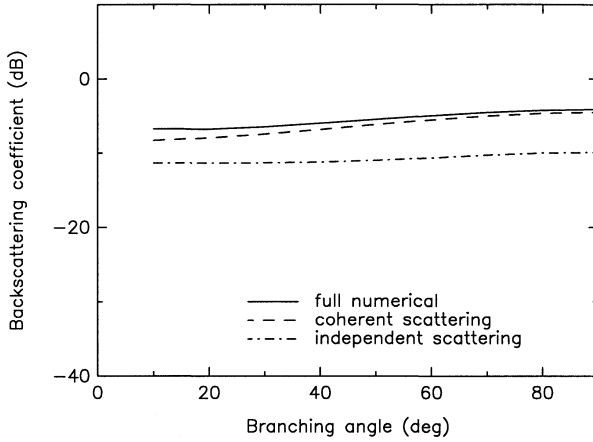

Figure 18. Backscattering coefficients for a two-layer medium $-\sigma_{hv}$ as a function of the center cylinder diameter. Fractional volume $f = 0.5\%$, $\epsilon_s = (11 + i4)\epsilon_0$. The scattering layer has a thickness $d = 0.25$ m and underlying half-space is flat and has permittivity $\epsilon_{soil} = (10 + i2)\epsilon_0$. Frequency is 5.3 GHz. Number of branches for the scatterers is 10.
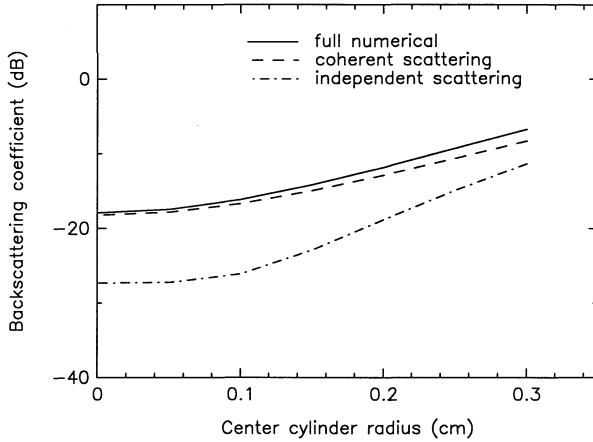
Figure 19. Backscattering coefficients for a two-layer medium $- \sigma_{vv}$ at nadir as a function of branching angle β. Fractional volume $f = 0.5\%$, $\epsilon_s = (11 + i4)\epsilon_0$. The scattering layer has a thickness $d = 0.25$ m and underlying half-space is flat and has permittivity $\epsilon_{soil} = (10 + i2)\epsilon_0$. Frequency is 5.3 GHz. Number of branches for the scatterers is 10.

Figure 20. Backscattering coefficients for a two-layer medium $- \sigma_{vv}$ as a function of the center cylinder diameter. Fractional volume $f = 0.5\%$, $\epsilon_s = (11 + i4)\epsilon_0$. The scattering layer has a thickness $d = 0.25$ m and underlying half-space is flat and has permittivity $\epsilon_{soil} = (10 + i2)\epsilon_0$. Frequency is 5.3 GHz. Number of branches for the scatterers is 10.

The co-polarized returns at nadir for the same set of scatterers are shown in Fig. 19. The difference between the exact solution from the coherent interaction model and the two other approximate solutions is smaller than that of the cross-polarized returns. The coherent addition approximation model gives a better estimate than the independent scattering model. The mutual interaction is small because of the small number of branches, and it is a weak function of the branching angle. When repeating the same calculation for various center cylinders, the results (Fig. 20) confirm that the mutual interaction is less important for co-polarized returns.

The difference between the coherent interaction solution and the coherent addition approximation becomes larger for a larger center cylinder. However, it is less significant for the co-polarized case than the cross-polarized case.

The coherent interaction solution for a single branching scatterer has been used to evaluate the scattering functions for the phase matrix and extinction matrix in the radiative transfer equations. The backscattering coefficients are then calculated from the iterative solution. The solution accounts for the multiple scattering effects within the cluster and single scattering between the clusters. It is well suited for the calculation of locally dense media such as vegetation canopies. The numerical solutions are then compared with the solutions obtained with different approximations. The results show that the coherent addition approximation gives a good estimate for co-polarized returns. For cross-polarized cases, both the independent and the coherent addition approximation models underestimate the backscattering returns. Cross-polarized returns are mainly due to the interaction between the components of the cluster and the two approximate methods do not account for this effect. By varying the branching angle of the cluster, it is shown that the mutual interaction is stronger for the smaller branching angle. The center cylinder in the cluster plays an important role in the cross-polarized returns. The triple bounce scattering mechanism, i.e. from branch to center cylinder back to branch, contributes to the high cross-polarized returns. It should be noted that in the cases studied, we want to isolate the contribution from mutual interaction for cross-polarized return, so only vertically oriented center cylinder is used. If some random orientation distribution for the clusters is introduced, the center cylinder, being larger than the branches, will contribute a significant cross-polarized return and the difference between the coherent

interaction model and the other two approximate methods may not be as markedly as reported here.

5.   Applications to Passive Remote Sensing

5.1 Vector Radiative Transfer Theory

In the area of remote sensing of geophysical terrains such as snow, ice and vegetation canopies, different theoretical models have been developed to model the electromagnetic response and to interpret experimental data. For the discrete scatterer model, the medium is considered to be a collection of discrete scatterers embedded in a homogeneous background. In the radiative transfer approach, independent scattering assumption has been used to evaluate the phase functions, the scattering coefficients and the absorption coefficients. The classical relations are that for N particles, the scattering cross section and absorption cross section of N particles are given by

$$(\sigma_s)_{ind} = \sum_{i=1}^{N} \sigma_{si} \qquad (65)$$

$$(\sigma_a)_{ind} = \sum_{i=1}^{N} \sigma_{ai} \qquad (66)$$

where ind stands for independent, and σ_{si} and σ_{ai} are respectively the scattering and absorption cross sections of the i th particle as it exists alone. For a medium with a high concentration of particles, independent scattering is not valid. Such high particle concentration media can be divided in two categories; uniformly dense media and locally dense media. For uniformly dense media, for example snow and ice, the fractional volume of the scatterers is high and the collective scattering effects can be described by the dense media theory [2, 7]. In vegetation canopies, the fractional volume of particles is low, usually between 0.1% to 0.5%. However, scatterers like branches and leaves can occur in clusters. They are regarded as locally dense media. In media that exhibit locally dense properties, collective scattering and absorption effects are important.

In this section, we focus on the effect of mutual interaction on the collective scattering and absorption in locally dense media. The ab-

sorption of the cluster can be several times greater than the incoherent sum of its components as predicted by equation (66).

The vector radiative transfer theory for passive remote sensing ia documented in the literature. We also use a cluster of branches as the primary scatterer. The vector radiative transfer equation that governs the propagation of the specific intensity $\overline{I}$ is given by

$$
\cos\theta \frac{d\overline{I}(\theta, \phi, z)}{dz} = -\overline{\overline{\kappa}}_e(\theta, \phi) \cdot \overline{I}(\theta, \phi, z)
$$
$$
+ \overline{\kappa}_a(\theta, \phi)CT + \int_{4\pi} d\Omega' \overline{\overline{P}}(\theta, \phi, \theta', \phi') \cdot \overline{I}(\theta'\phi', z)
\tag{67}
$$

where $\overline{\overline{\kappa}}_e$ is the extinction matrix for the Stokes vector due to the scatterer that accounts for losses from scattering and absorption, $\overline{\kappa}_a$ is the absorption coefficient vector, $\overline{\overline{P}}(\theta, \phi, \theta', \phi')$ is the phase matrix which relates the scattered intensities in the direction of (θ, ϕ) to the incident intensities in the direction of (θ', ϕ'), T is the physical temperature, and C is a constant given by

$$
C = \frac{K}{\lambda^2}
\tag{68}
$$

with K as the Boltzmann's constant (1.38×10^{-23} J/K) and λ the free space wavelength. The absorption vector can be expressed in terms of the number density of the scatterers and the absorption cross sections as follows

$$
\overline{\kappa}_a(\theta, \phi) = n_o \begin{bmatrix} \sigma_{a1}(\theta, \phi) \\ \sigma_{a2}(\theta, \phi) \\ \sigma_{a3}(\theta, \phi) \\ \sigma_{a4}(\theta, \phi) \end{bmatrix}
\tag{69}
$$

5.2 Absorption Enhancement

The geometrical configuration of the cylinder cluster is shown in Fig. 10. The cluster has the same parameters as described in Section 4.2. All the quantities of the absorption cross section are normalized by dividing by the independent scattering absorption cross section $(\sigma_a)_{ind}$ as given by equation (66) for the horizontal polarization at incidence angle of 90°. The frequency is 5.3 GHz.

In the first case, we consider such a cluster with 10 branches. The variation of absorption cross section with incidence angle θ for two polarizations is shown in Figs. 21 and 22.
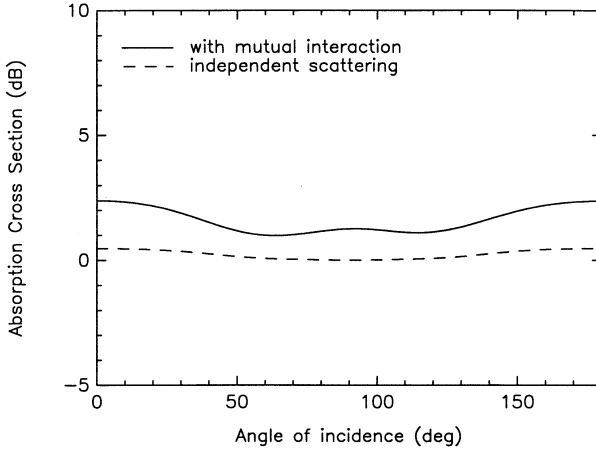

Figure 21. Absorption cross section as a function of incidence angle for horizontal polarization. Number of branches is 10. Curves are normalized by $(\sigma_{ah}(90°))_{ind}$ with the numerical value of -39.5 dBsm.
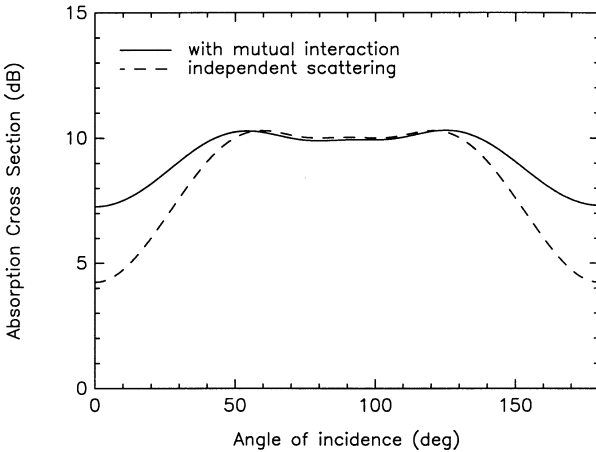

Figure 22. Absorption cross section as a function of incidence angle for vertical polarization. Number of branches is 10. Curves are normalized by $(\sigma_{ah}(90°))_{ind}$ with the numerical value of -39.5 dBsm.

At nadir, there is a difference between two polarizations. The cluster exhibits azimuthal asymmetry due to a few number of branches. It should be noted that the center cylinder is much larger than the branching ones and the effect of the center cylinder is dominant in this case. The absorption cross section for the horizontal polarization obtained from independent scattering model is not sensitive to the changes in the incidence angle. This is because the absorption is proportional to the square of the magnitude of the internal field and the incident electric field vector does not change with incidence angle for horizontal polarization.

The small variation with incidence angle is due to the contribution from the branches. If there are enough branches to exhibit azimuthal symmetry, such variations will diminish. The variation with incidence angle is much larger for the vertical polarization case because the incident electric field vector changes with the incidence angle. The difference between the present model and the independent scattering model is due to the mutual interactions between the components of the cluster. The vertical polarization case has a large enhancement at nadir. The internal field from the independent scattering model can be regarded as the first order internal field. The incident electric field has a small tangential component on the center cylinder and hence a small first order internal field. However, the induced fields on the branches can generate a larger tangential component on the center cylinder which facilitates the penetration of the electric field into the center cylinder. This mutual interaction creates a significant change in the internal field and the absorption is several times larger than that of the independent scattering case. At 90° incidence angle, the first order internal field for the center cylinder is already high and the enhancement is not significant.

The second case we consider is a cluster with 48 branches. The number of branching layers has been increased to 12. Within each layer, four branches are arranged at right angles to each other. They are then attached to the center cylinder at random azimuthal locations. The results are shown in Figs. 23 and 24.
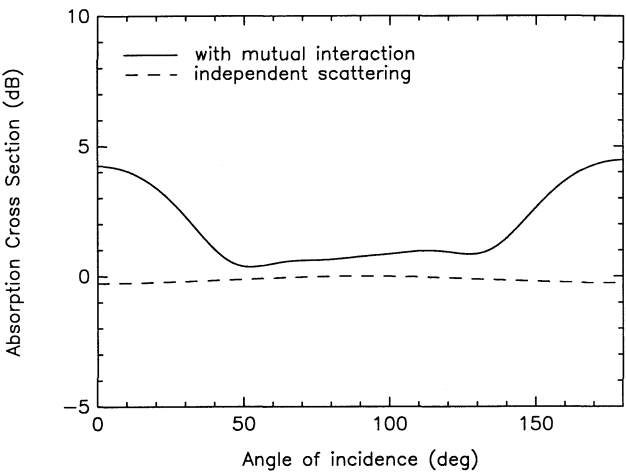
Figure 23. Absorption cross section as a function of incidence angle for horizontal polarization. Number of branches is 48. Curves are normalized by $(\sigma_{ah}(90°))_{ind}$ with the numerical value of -30.7 dBsm.
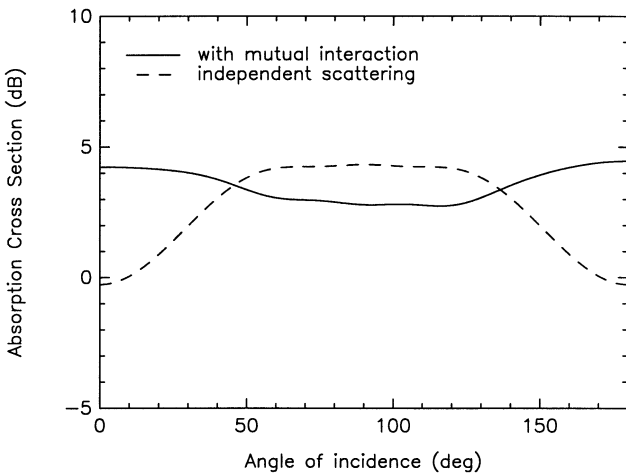

Figure 24. Absorption cross section as a function of incidence angle for vertical polarization. Number of branches is 48. Curves are normalized by $(\sigma_{ah}(90°))_{ind}$ with the numerical value of -30.7 dBsm.

We observe that the cluster exhibits azimuthal symmetry due to the large number of branches. The results at nadir for the two polarizations are approximately the same. In Fig. 23, as predicted previously, the independent scattering curve for the horizontal polarization does not change with incidence angle. Significant enhancements are observed for both polarizations at nadir. However, for the vertical polarization, the absorption with mutual interaction is less than that from independent scattering at large incidence angles. This is due to the blocking of the center cylinder and the branches which results in lower internal fields. The horizontal polarization only excites a small internal field for the center cylinder, so that the near field interaction always enhances the absorption. Without considering the structure of cluster, the independent scattering predicts a symmetric absorption cross section with 90° incidence angle. It should be noted that even though the absorption cross section does not obey inversion symmetry, the extinction cross section does. The explanation is that, by combining optical theorem and reciprocity, we obtain

$$
\begin{aligned}
\sigma_e(\theta) &= \frac{4\pi}{k}\,\mathrm{Im}(f_{pp}(\theta;\theta)) = \frac{4\pi}{k}\,\mathrm{Im}(f_{pp}(\pi-\theta;\pi-\theta)) \\
&= \sigma_e(\pi-\theta)
\end{aligned}
\tag{70}
$$

where k is the wavenumber, σ_e is the extinction cross section, f_{pp} is the forward scattering function and $p = v, h$. The extinction cross sections show the inversion symmetry in Figs. 25 and 26.

The extinction cross sections are calculated from the optical theorem. Energy conservation is observed in the calculation to 99% accuracy.

To study the relative importance of the absorption enhancement and blocking, we repeat the case 2 with the center cylinder removed. The results are shown in Figs. 27 and 28.

Blocking lowers the internal fields of all the branches, and without the center cylinder, no significant enhancement is made for the horizontal polarization to counter the effect of blocking. Therefore at large incidence angles, the absorption from the numerical model is lower than that of the independent scattering model for both polarizations.
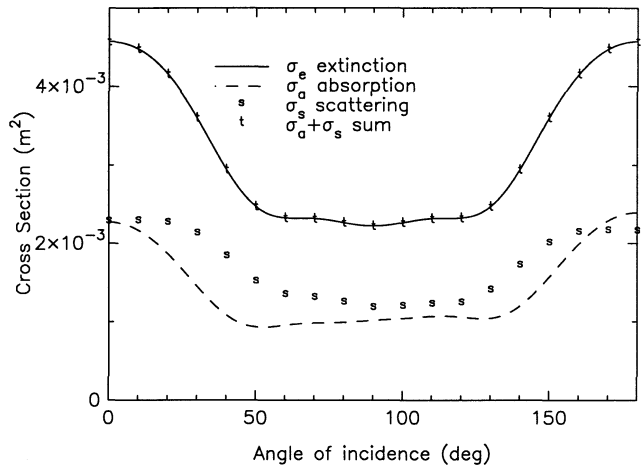
Figure 25. Cross sections as a function of incidence angle for horizontal polarization. Number of branches is 48.
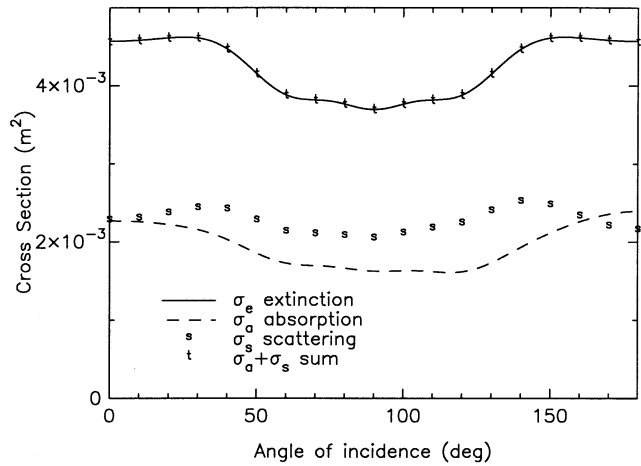

Figure 26. Cross sections as a function of incidence angle for vertical polarization. Number of branches is 48.
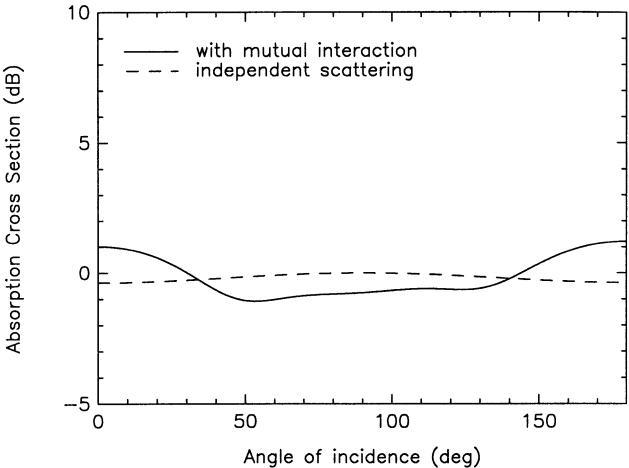
Figure 27. Absorption cross section as a function of incidence angle for horizontal polarization. Number of branches is 48. Center cylinder is removed from the cluster. Curves are normalized by $(\sigma_{ah(90°)})_{ind}$ with the numerical value of -30.9 dBsm.
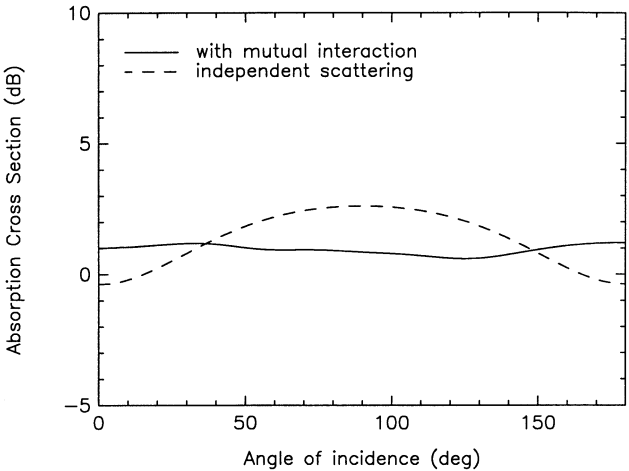

Figure 28. Absorption cross section as a function of incidence angle for vertical polarization. Number of branches is 48. Center cylinder is removed from the cluster. Curves are normalized by $(\sigma_{ah(90°)})_{ind}$ with the numerical value of -30.9 dBsm.

5.3 Brightness Temperature Calculation

In this section, theoretical results based on the MoM calculation of the scattering function of the scatterer are presented and compared with results obtained from approximate methods. The brightness temperature is calculated for a two-layer medium embedded with vertically oriented clusters with a flat bottom surface. The configuration of the problem is similar to that of (Fig. 11) with the incidence angle replaced by the observation angle. The phase matrix is evaluated in three different ways. First, it is calculated by the MoM for the cluster, in which the interactions between all components are fully accounted for (coherent interaction model). It is then compared with the independent scattering model in which the incoherent sum of its components is used to evaluate the phase matrix and the extinction matrix (independent scattering model). The third method is the coherent addition approximation [8]. The phase matrix is evaluated using this model and the extinction matrix is calculated by the addition of the absorption cross section and the total scattering cross section.

In the first case, the brightness temperature for a half-space configuration with vertically oriented scatterers is calculated. The 10-branch scatterer described in the previous section is used. Ten realizations are generated for the branching scatterers to obtain the average brightness temperature. The radiometer frequency is 5.3 GHz. The canopy has a fractional volume $f = 0.5\%$ and a permittivity $\epsilon_s = (11 + i4)\epsilon_o$. The physical temperature of the canopy is 300 K. The results for vertical and horizontal polarizations are shown in Figs. 29 and 30.

The brightness temperature for the half-space medium is closely related to the ratio of the absorption coefficient κ_a and the extinction coefficient κ_e. These two quantities are functions of the observation angle. The extinction coefficient κ_e is equal to the sum of the scattering coefficient κ_s and the absorption coefficient κ_a. As mentioned in the previous section, for the 10-branch case, absorption enhancement is observed. The independent scattering model gives the highest brightness temperature because it ignores the coherent effect and yields the lowest scattering coefficient. Although it gives a low κ_a, it does not completely compensate for the underestimation of κ_s. As a result, the ratio of the κ_a/κ_e is highest among the three methods. When the scattering coefficient is calculated by the coherent addition approxi-

mation, it has a higher value than the independent scattering model. With κ_a obtained from the independent scattering model, it has a lower ratio of κ_a/κ_e, and hence lower brightness temperature [22]. The coherent addition approximation model provides a good estimate of the brightness temperature for the vertical polarization. It underestimates the brightness temperature for the horizontal polarization at low observation angles because it does not account for the absorption enhancement, which is particularly high at that range.

The thermal emission from the two-layer configuration modeling a vegetation canopy overlying on a flat ground surface is also calculated (case 2). The permittivity of the ground is $\epsilon_{soil} = (16+i4)\epsilon_o$ while the ground and the canopy temperatures are both 300 K. The thickness (d) of the vegetation canopy is 25 cm. The optical depth $\kappa_e d/\cos\theta$ varies for different models. The coherent interaction model gives the highest optical depth while the independent scattering model gives the lowest. The optical depth indicates how well the overlying layer shields the half-space underneath. Figs. 31 and 32 show the brightness temperatures for the two polarizations.

With the interaction between surface and volume scattering, the brightness temperatures obtained from the coherent interaction model can be higher than the other two approximate methods, depending on the properties of the ground surface and the canopy thickness. The brightness temperature of the horizontal polarization decreases with increasing observation angle at that range. As the observation angle increases, the optical depth increases and the half-space limit is approached. This explains why the brightness temperature for the horizontal polarization rises at large observation angles.

The effect of canopy thickness is studied by varying it from 10 cm and 100 cm. The brightness temperatures observed at 8.4^o are shown in Figs. 33 and 34.
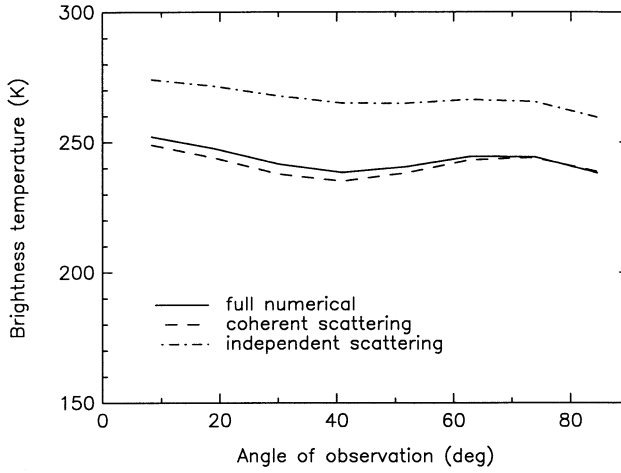
Figure 29. Brightness temperature of a half-space medium embedded with vertically oriented scatterers $- T_{Bh}, f = 0.5\%, \epsilon_s = (11 + i4)\epsilon_0$. Frequency is 5.3 GHz. Number of branches is 10.
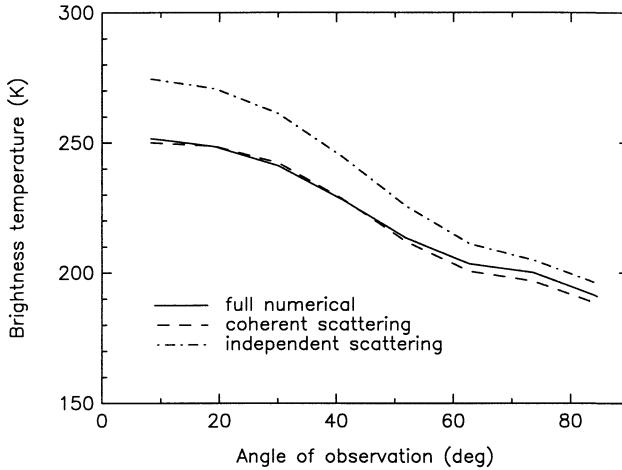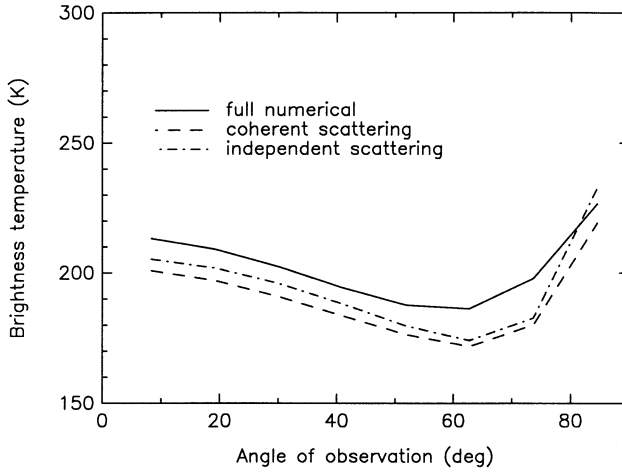

Figure 30. Brightness temperature of a half-space medium embedded with vertically oriented scatterers $- T_{Bv}, f = 0.5\%, \epsilon_s = (11 + i4)\epsilon_0$. Frequency is 5.3 GHz. Number of branches is 10.

Figure 31. Brightness temperature of a two-layer medium − $T_{Bh}, f = 0.5\%, \epsilon_s = (11 + i4)\epsilon_0$. **Scattering layer has a thickness** $d = 0.25$ **m and underlying half-space is flat and has a permittivity** $\epsilon_{soil} = (16 + i4)\epsilon_0$. **Frequency is 5.3 GHz. Number of branches is 10.**
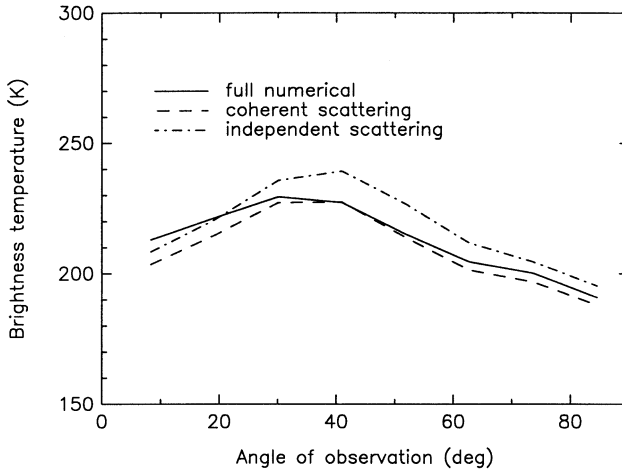

Figure 32. Brightness temperature of a two-layer medium − $T_{Bv}, f = 0.5\%, \epsilon_s = (11 + i4)\epsilon_0$. **Scattering layer has a thickness** $d = 0.25$ **m and underlying half-space is flat and has a permittivity** $\epsilon_{soil} = (16 + i4)\epsilon_0$. **Frequency is 5.3 GHz. Number of branches is 10.**
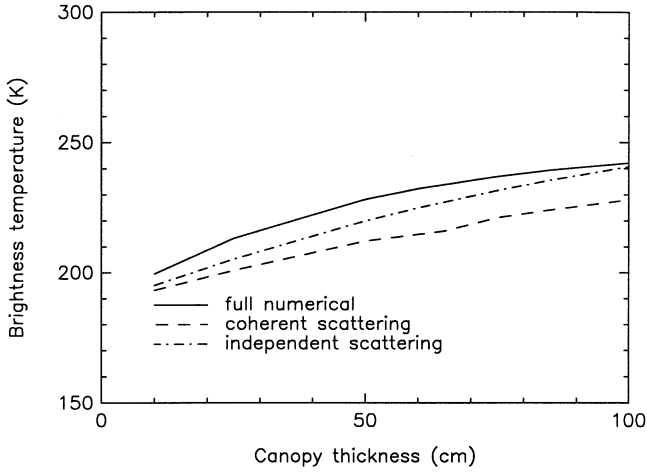
Figure 33. Brightness temperature of a two-layer medium $- T_{Bh}$ **at observation angle** $= 8.4°$, $f = 0.5\%, \epsilon_s = (11 + i4)\epsilon_0$. **Underlying half-space is flat and has a permittivity** $\epsilon_{soil} = (16 + i4)\epsilon_0$. **Frequency is 5.3 GHz. Number of branches is 10.**

Figure 34. Brightness temperature of a two-layer medium $- T_{Bv}$ **at observation angle** $= 8.4°$, $f = 0.5\%, \epsilon_s = (11 + i4)\epsilon_0$. **Underlying half-space is flat and has a permittivity** $\epsilon_{soil} = (16 + i4)\epsilon_0$. **Frequency is 5.3 GHz. Number of branches is 10.**
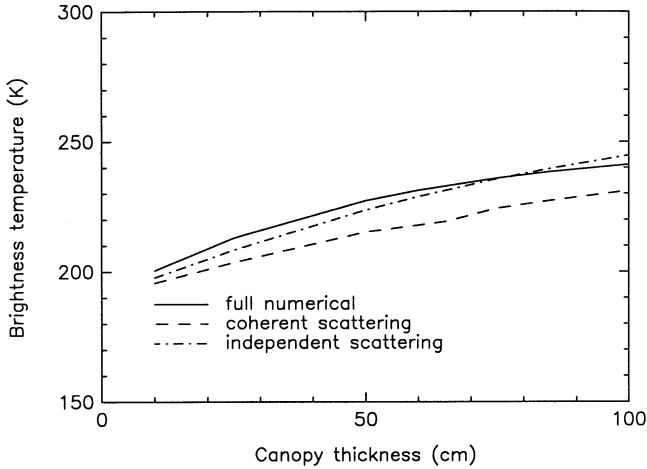
The brightness temperatures from the coherent interaction model in this case are higher than the two approximate methods when the canopy thickness is small because it shields the bottom half-layer more effectively. The difference decreases as the thickness of the canopy increases. As the half-space limit is approached, the brightness temperatures from coherent interaction model fall between that of independent scattering model and the coherent addition approximation model.

A 48-branch scatterer described in the previous section is used in the brightness temperature calculation (case 3). The same parameters as the previous case are used. The scatterer has a more complicated structure, and both blocking and absorption enhancement occur. The brightness temperatures for a canopy thickness of 25cm are shown in Figs. 35 and 36.

In general, the coherent addition approximation in these cases gives a good estimate of the brightness temperatures. The difference between the coherent interaction model and the coherent addition approximation for vertical polarization at large observation angles in the two-layer medium is larger due to the inaccuracy in the optical depth.

As mentioned in the previous section, when the branching angle is small, the mutual interactions will be strong and the coherent interaction model will give the most accurate results. To illustrate the point, the 48 branch-clusters with branching angles of 15° and 75° are used in the calculation. All other parameters remain the same as the previous cases. The brightness temperatures of the vertical polarization with 15° and 75° branching angle clusters for a two-layer medium of thickness 25 cm are shown in Figs. 37 and 38, respectively. The difference between models can be as large as 30K for some observation angles.
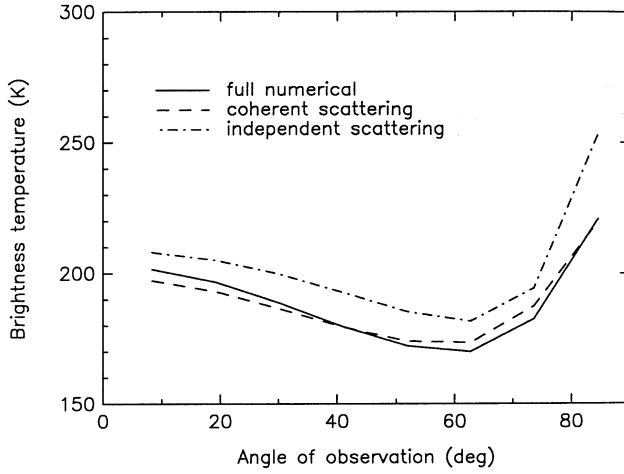
Figure 35. Brightness temperature of a two-layer medium $- T_{Bh}, f =$ $0.5\%, \epsilon_s = (11 + i4)\epsilon_0$. **Scattering layer has a thickness** $d = 0.25$ **m and underlying half-space is flat and has a permittivity** $\epsilon_{soil} = (16 + i4)\epsilon_0$. **Frequency is 5.3 GHz. Number of branches is 48.**

Figure 36. Brightness temperature of a two-layer medium $- T_{Bv}, f =$ $0.5\%, \epsilon_s = (11 + i4)\epsilon_0$. **Scattering layer has a thickness** $d = 0.25$ **m and underlying half-space is flat and has a permittivity** $\epsilon_{soil} = (16 + i4)\epsilon_0$. **Frequency is 5.3 GHz. Number of branches is 48.**
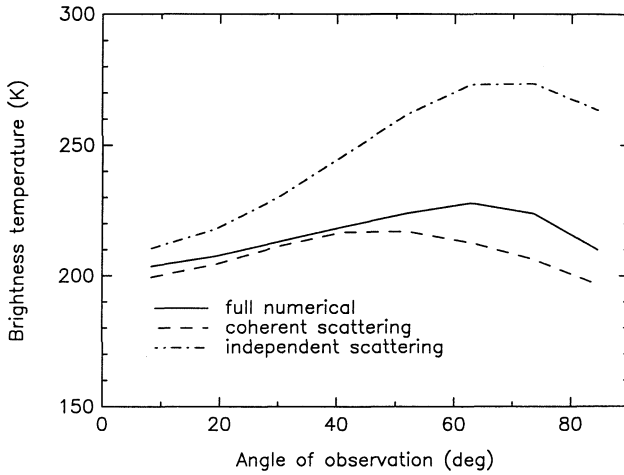
Figure 37. Brightness temperature of a two-layer medium $-$ $T_{Bv}, f = 0.5\%, \epsilon_s = (11 + i4)\epsilon_0$. Scattering layer has a thickness $d=$ 0.25 m and underlying half-space is flat and has a permittivity $\epsilon_{soil} = (16 + i4)\epsilon_0$. Frequency is 5.3 GHz. Number of branches is 48. Branching angle β is $15°$.
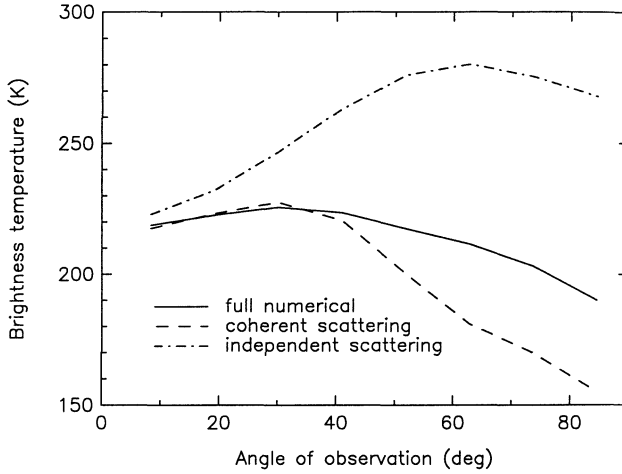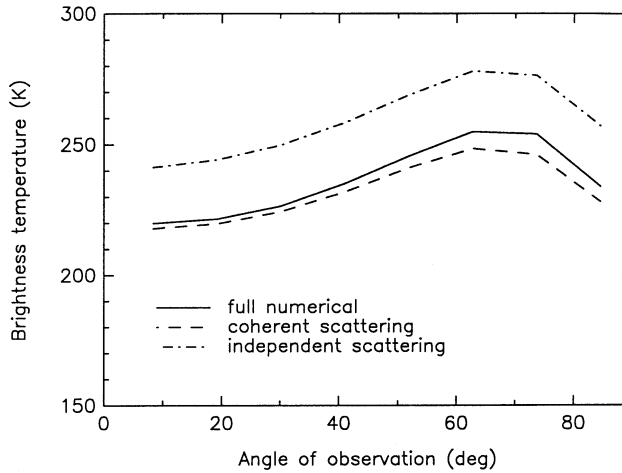

Figure 38. Brightness temperature of a two-layer medium $-$ $T_{Bv}, f = 0.5\%, \epsilon_s = (11 + i4)\epsilon_0$. Scattering layer has a thickness $d=$ 0.25 m and underlying half-space is flat and has a permittivity $\epsilon_{soil} = (16 + i4)\epsilon_0$. Frequency is 5.3 GHz. Number of branches is 48. Branching angle β is $75°$.

6.   Conclusion

In this paper, we studied the effect of mutual interaction in the scattering behavior of locally dense vegetation. The radiative transfer theory is modified by defining the phase matrix and extinction coefficient as, respectively, the bistatic cross section per unit volume of space and the extinction cross section per unit volume of space. The limit of the volume of space is taken such that the collective scattering effects of the particles within the volume are taken into account. The scattering functions of the scatterers within the volume of space are obtained from the numerical solution of Maxwell's equations, and hence all the interactions between different components of the cluster are retained. Because of low fractional volume, the interaction between two remotely separated primary scatterers is small, thus the use of radiative transfer theory is justified. Analytical iterative solution method is used in the active case to calculate backscattering coefficients and Gaussian quadrature method is used in the passive case to calculate brightness temperatures.

A better understanding of the clustering effects is obtained through the numerical investigation. For scatterers with large number of branches, the independent model is shown to be inadequate. The coherent addition approximation for branching structure improves the estimate of the scattering characteristics. However, since the internal field in the model is assumed to be the same as the independent scattering model, mutual interaction is not included. Using the MoM approach, it is shown that both the absorption and the scattering losses are enhanced by mutual interaction.

In this paper, we have shown that the coherent interaction model provides accurate solutions when mutual interaction is strong, which cannot be handled with existing approximate methods. Suggestions for future work are to improve modeling of locally dense medium with both analytical and numerical approaches. Coherent addition approximation model provided reasonable results in some cases. It may be possible to improve the model by incorporating high order terms to account for mutual interaction. Only thin cylinder structures have been studied for the clustering effects in this chapter. A possible extension is to study scatterers with different structures, for example, discs and thick cylinders.

References

1. Tsang, L., J. A. Kong, Z. Chen, K. Pak, and C. Hsu, "Theory of microwave scattering from vegetation on the collective scattering effects of discrete scatterers," *Proceedings of the ESA NASA Workshop on Passive Microwave Remote Sensing of Land-Atmosphere Interaction,* VSP Press, Netherlands, 1993.

2. Tsang, L., J. A. Kong, and R. T. Shin, *Theory of Microwave Remote Sensing,* Wiley-Interscience, New York, 1985.

3. Ulaby, F. T., R. K. Moore, and A. K. Fung, *Microwave Remote Sensing: Active and Passive,* Addison-Wesley, Reading, 1981.

4. Ulaby, F. T., and C. Elachi (eds.), *Radar Polarimetry for Geoscience Applications,* Artech. House, Norwood, 1990.

5. Wen, B., L. Tsang, D. P. Winebrenner, and A. Ishimaru, "Dense medium radiative transfer theory: comparison with experiment and application to microwave remote sensing polarimetry," *IEEE Transactions on Geoscience and Remote Sensing,* Vol. 28, No. 1, 46–59, 1990.

6. Tsang, L., "Passive remote sensing of dense nontenuos media," *Journal of Electromagnetic Waves and Applications,* Vol. 1, No. 2, 159–174, 1987.

7. Tsang, L., "Dense media radiative transfer theory for dense discrete random media with spherical particles of multiple sizes and permittivities," *Progress in Electromagnetic Research,* Vol. 6, Ch. 5, Elsevier, New York, 1992.

8. Yueh, H. A., J. A. Kong, J. K. Jao, R. T. Shin, and T. LeToan, "Branching model for vegetation," *IEEE Transactions on Geoscience and Remote Sensing,* Vol. 30, No. 2, 390–402, 1992.

9. Hsu, C. C., H. C. Han, R. T. Shin, J. A. Kong, A. Beaudoin, and LeToan, T., "Radiative transfer theory for polarimetric remote sensing of pine forest at P-band," *International Journal of Remote Sensing,* Vol. 15, No. 14, 1994.

10. Hsu, C. C., R. T. Shin, J. A. Kong, A. Beaudoin, and T. LeToan, "Application of theoretical model for microwave remote sensing of forest," *Proceedings IGARSS 93,* Tokyo, 1993.

11. Hsu, C. C., W. C. Au, J. A. Kong, and L. Tsang, "Theoretical model for remote sensing for vegetation," *URSI Conference Proceedings,* University of Kansas, 1994.

12. Au, W. C., L. Tsang, and J. A. Kong, "Absorption enhancement of scattering electromagnetic waves by dielectric cylinder clusters," *Microwave and Optical Technology Letters,* Vol. 7, No. 10, 454–457, 1994.

13. Tsang, L., C. H. Chan, and H. Sangani, "Banded matrix iterative approach to Monte Carlo simulations of scattering of waves by large-scale random rough surface problems: TM case," *Electronics Letters,* Vol. 29, No. 2, 166–167, 1993.

14. Tsang, L., C. H. Chan, and K. Pak, "Monte Carlo simulations of a two-dimensional random surface using the sparse-matrix flat-surface iterative approach" *Electronics Letters,* Vol. 29, No. 13, 1153–1154, 1993.

15. Tsang, L., C. E. Mandt, and K. H. Ding, "Monte Carlo simulations of the extinction rate of dense media with randomly distributed dielectric spheres based on solution of Maxwell's equations," *Optics Letters,* Vol. 17, No. 5, 1992.

16. Lu, C. C., Y. M. Wang, W. C. Chew, and L. Tsang, "The application of recursive aggregate T-matrix algorithm in the Monte Carlo simulations of the extinction rate of random particles," *Proceedings of IEEE Antenna and Propagation Symposium,* Ann Arbor, 1993.

17. Wang, J. J. H., *Generalized Moment Methods in Electromagnetics – Formulation and Computer Solution in Integral Equations,* John Wiley & Sons, New York, 1991.

18. Chew, W., *Electromagnetic Waves and Fields in Inhomogeneous Media,* Van Nostrand Reinhold, New York, 1990.

19. Yaghjian, A. D., "Electric dyadic Green's functions in the source region," *Proceedings of IEEE,* Vol. 68, No. 2, 248–263, 1980.

20. Howard, A. Q., and D. B. Seidel, "Singularity extraction in kernel functions in a closed region problem," *Radio Science,* Vol. 13, No. 3, 425–430, 1978.

21. Lee, S., J. Boersma, C. Law, and G. A. Deschamps, "Singularity in Green's function and its numerical evaluation," *IEEE Transactions on Antennas and Propagation,* Vol. 28, No. 3, 311-317, 1980.

22. Au, W. C., *Computational Electromagnetics in Microwave Remote Sensing,* Ph.D. thesis, Massachusetts Institute of Technology, Department of Aeronautics and Astronautics, 1994.

23. Draine, B. T., "The discrete-dipole approximation and its application to interstellar graphite grain," *The Astrophysical Journal,* Vol. 333, 848–872, 1988.

24. Wu, T. K., and L. L. Tsai, "Scattering from arbitrarily-shaped lossy dielectric bodies of revolution," *Radio Science,* Vol. 12, No. 5, 709–718, 1977.

25. Mougin, E., A. Lopes, and T. LeToan, "Microwave propagation at X band in cylindrical-shaped forest components: attenuation observations," *IEEE Transactions on Geoscience and Remote Sensing,* Vol. 28, No. 1, 60–69, 1990.

26. Lang, R. H., "Electromagnetic backscattering from a sparse distribution of lossy dielectric scatterers," *Radio Science,* Vol. 16, No. 1, 15–30, 1981.

27. Ishimaru, A., and C. W. Yeh, "Matrix representation of the vector radiative transfer equations for randomly distributed nonspherical particles," *Journal of the Optical Society of America A,* Vol. 1, No. 4, 359–364, 1984.

28. Mougin, E., and A. Lopes, "Microwave propagation at X band in cylindrical-shaped forest components: interpretation of attenuation observations," *IEEE Transactions on Geoscience and Remote Sensing,* Vol. 28, No. 3, 315–342, 1990.

29. Ulaby, F. T., and M. A. El Rayes, "Microwave dielectric spectrum of vegetation. Part II: Dual-dispersion model," *IEEE Transactions on Geoscience and Remote Sensing,* Vol. 25, No. 5, 550–556, 1987.